An Improved Virtual Inertia Control for Three-Phase Voltage Source Converters Connected to a Weak Grid

Fang, Jingyang; Lin, Pengfeng; Li, Hongchang; Yang, Yongheng; Tang, Yi

Published in:
I E E E Transactions on Power Electronics

DOI (link to publication from Publisher):
10.1109/TPEL.2018.2885513

Publication date:
2019

Document Version
Accepted author manuscript, peer reviewed version

This article has been accepted for publication in a future issue of this journal, but has not been fully edited. Content may change prior to final publication. Citation information: DOI 10.1109/TPEL.2018.2885513, IEEE Transactions on Power Electronics

An Improved Virtual Inertia Control for Three-Phase Voltage Source Converters Connected to a Weak Grid

Jingyang Fang, *Student Member*, *IEEE*, Pengfeng Lin, *Student Member*, *IEEE*, Hongchang Li, *Member*, *IEEE*, Yongheng Yang, *Senior Member*, *IEEE*, Yi Tang, *Senior Member*, *IEEE*

***Abstract*—The still increasing share of power converter-based renewable energies weakens the power system inertia. The lack of inertia becomes a main challenge to small-scale modern power systems in terms of control and stability. To alleviate such adverse effects from inertia reductions, e.g., undesirable load shedding and cascading failures, three-phase grid-connected power converters should provide virtual inertia upon system demands. This can be achieved through directly linking the grid frequency and voltage references of DC-link capacitors/ultracapacitors. This paper reveals that the virtual inertia control may possibly induce instabilities to the power converters under weak grid conditions, which is caused by the coupling between the *d*- and *q*-axis as well as the inherent differential operator introduced by the virtual inertia control. To tackle this instability issue, this paper proposes a modified virtual inertia control to mitigate the differential effect, and thus alleviating the coupling effect to a great extent. Experimental verifications are provided, which demonstrate the effectiveness of the proposed control in stabilizing three-phase grid-connected power converters for inertia emulation even when connected to weak grids.**

***Index Terms*—Frequency regulation, renewable energy, stability, virtual inertia, weak grid, power converter.**

I. INTRODUCTION

THE main driving forces to deploy and develop a large amount of renewable energies integrated into modern power systems include the reduction of carbon footprint and increment of clean energy production [1]. Despite being pursued worldwide, the employment of renewable energies even partly to replace fossil fuels (expected to completely phase out in the future) may retrofit the entire power grid and challenge the stability of modern power systems [2]. One of the major concerns, which has already been acknowledged in small-scale power systems, e.g., in Ireland and Great Britain, refers to the frequency instability due to the lack of inertia in the system with a high penetration level of power converter-interfaced renewable energies [3].

In conventional power systems, synchronous generators operating at a speed in synchronism with the grid frequency act as the major grid interfaces [4]. When a frequency change due to the power imbalance between generation and demand occurs, synchronous generators autonomously slow down or speed up in accordance with the grid frequency. In this way, the synchronous generators release/absorb the energy to/from the power grid so that the power mismatch can partially be compensated. This effect is quantitatively evaluated by the per unit kinetic energy, which is defined as power system inertia [4], [5]. However, this phenomenon changes in modern power systems, because most of renewable energy sources (RESs), such as wind energies and solar photovoltaics (PV), are coupled to the power grid through power electronic converters [1], [6]. Different from synchronous generators, grid-connected power converters normally operate in the maximum power point tracking (MPPT) mode to optimize the energy yield without any inertia contribution [7]. This is because there is no kinetic energy in such power conversion systems that can be used as rotational inertia [8]. As more synchronous generators are phasing out and being replaced by power converters, the entire power system becomes more inertia-less, being a major concern for stability and control. More specifically, without sufficient inertia, the grid frequency and/or the rate-of-change-of-frequency (RoCoF) may be apt to go beyond the acceptable range under severe frequency events, leading to generation tripping, undesirable load shedding, or even system collapses [9].

Various solutions to tackle the lack of inertia issue have already been proposed in the literature. One straightforward approach is to change the requirements of RoCoF withstand capabilities of generators [3]. Although this solution has been accepted as an efficient and suitable solution by the system operators in Ireland/North Ireland [10], the high costs associated with generator testing mainly hinder its wide applications. In addition, since this solution involves no effort

Manuscript received June 06, 2018; revised September 03, 2018 and October 31, 2018; accepted December 04, 2018. This research is supported by the National Research Foundation, Prime Minister's Office, Singapore under the Energy Innovation Research Programme (EIRP) Energy Storage Grant Call and administrated by the Energy Market Authority (NRF2015EWT-EIRP002-007). The paper has been presented in part in [43]. (*Corresponding author: Yi Tang*)

J. Fang and Y. Tang are with the School of Electrical and Electronic Engineering, Nanyang Technological University, Singapore 639798 (e-mail: jfang006@e.ntu.edu.sg; yitang@ntu.edu.sg).

H. Li and P. Lin are with the Energy Research Institute @ NTU (ERI@N), Nanyang Technological University, Singapore 639798 (e-mail: hongchangli@ntu.edu.sg; linp0010@e.ntu.edu.sg;).

Y. Yang is with the Department of Energy Technology, Aalborg University, Aalborg 9220, Denmark (e-mail: yoy@et.aau.dk).

This article has been accepted for publication in a future issue of this journal, but has not been fully edited. Content may change prior to final publication. Citation information: DOI 10.1109/TPEL.2018.2885513, IEEE Transactions on Power Electronics

for inertia enhancement, the inertia issue cannot be completely resolved. Another possibility for inertia enhancement is the use of synchronous condensers, i.e., synchronous generators without prime movers or loads [11]. However, high capital and operating costs have deterred the widespread adoption of synchronous condensers.

Similar to synchronous generators, wind turbines also feature rotating masses and the associated kinetic energy. However, their rotating speeds are usually decoupled from the grid frequency for a better speed control to optimize the energy harvesting [12], [13]. In this regard, variable-speed wind generation systems normally contribute zero synchronous inertia to the power grid. To exploit the stored kinetic energy in wind turbines, the electromagnetic torque (or grid-injected power) can be changed in response to the grid frequency during frequency events [13]. Through this approach, the emulated inertia or virtual inertia will be synthesized by wind turbines. In [14], the electromagnetic torque is proportionally linked to the RoCoF (i.e., df / dt) for inertia emulation. References [15−17] propose several modified virtual inertia controls without considering the aerodynamics and speed recovery processes of wind turbines. As analyzed by [18] and [19], speed recovery processes will greatly change the inertia response of wind turbines and may cause a recurring frequency dip or even rotor stall. As such, the emulated inertia from wind turbines and synchronous inertia are still not identical, as proven by the wind inertial response in Hydro-Quebec [3].

Another emerging approach aims to generate virtual inertia through battery storage systems. This can be achieved by introducing a proportional link between RoCoF (i.e., df / dt) and battery power references [20−22]. As mentioned, similar inertia emulation schemes have already been applied to wind turbines [23], [24]. The formulation of battery power references necessitates the fast and accurate detection of RoCoF signals, which is considered as a significant challenge by the power system operators in Ireland and Great Britain [3]. To tackle this issue, the possibility of using a frequency-locked-loop (FLL) for RoCoF detection is discussed in [21]. In addition, it is revealed that power converters may have instability concerns when adopting the df / dt-based inertia emulation scheme [25], [26]. Furthermore, slow inertia emulation (which can be achieved through the use of a first-order lag of a time constant around 1 s) can address the instability concerns [26]. The analysis and conclusion provided in [26] are of great importance and can provide useful guidelines for virtual inertia design.

As compared to batteries, ultracapacitors feature a higher power density and are therefore suitable for inertia emulation [27]. In addition to ultracapacitors, capacitors are normally necessary in the DC-links of grid-connected power converters for voltage support and harmonic filtering [28]. These capacitors may also be exploited to reap the benefit of their capabilities for inertia emulation with a small or even no change of hardware [29], [30]. Regarding control implementations, the inertia emulated by capacitors and ultracapacitors are very similar. Because of adjustable capacitor and ultracapacitor voltages, RoCoF detection is no longer necessary. By proportionally linking the capacitor voltage and the grid frequency, virtual inertia can be expected from the capacitors/ultracapacitors [29], [31], [32]. This approach can be very effective and simple in terms of control designs. Therefore, it has been regarded as a promising solution and extended to high-voltage direct current (HVDC) applications such as modular multilevel converters (MMCs) [33−35].

It is known that weak grids featuring large grid impedances may make three-phase grid-connected power converters unstable due to the resonance caused by high-order passive filters [36], coupling among multiple power converters [37], and influence of the phase-locked-loop (PLL) on the current control [38]. In addition to the above-mentioned causes, this paper reveals that the strong coupling between the control loops (i.e., the dq-reference control systems) and the differential operator are responsible for the instability of grid-connected power converters with virtual inertia from capacitors/ultracapacitors.

The rest of this paper is organized as follows. Section II presents the concept of virtual inertia and the fundamentals of three-phase power converters with the virtual inertia control. With the system models, the instability issue is further explored in Section III. Section IV introduces the proposed modified virtual inertia control for stability enhancement. The effectiveness of the proposed control to enhance the stability under weak grids is experimentally verified in Section V. Finally, Section VI provides the concluding remarks.

II. Three-Phase Grid-Connected Power Converters with Virtual Inertia Control

Power electronics is the key to renewable energy integration, and power converters as grid interfaces are replacing conventional synchronous generators. However, presently, the power system inertia is solely contributed by the rotating masses of synchronous generators. As a result, the lack of inertia may challenge the operation and control of modern power systems [3], [9].

A. Concept of Virtual Inertia

To address the issue of less inertia in more-electronics power systems, capacitors and/or ultracapacitors have been increasingly exploited to absorb/release power in a similar way as conventional synchronous generators do in the case of frequency events for inertia emulation [29−32]. Fig. 1 illustrates the mapping between the synchronous generator and the capacitor, where the inertia constant of the synchronous generator H is defined as the ratio of the kinetic

This article has been accepted for publication in a future issue of this journal, but has not been fully edited. Content may change prior to final publication. Citation information: DOI 10.1109/TPEL.2018.2885513, IEEE Transactions on Power Electronics

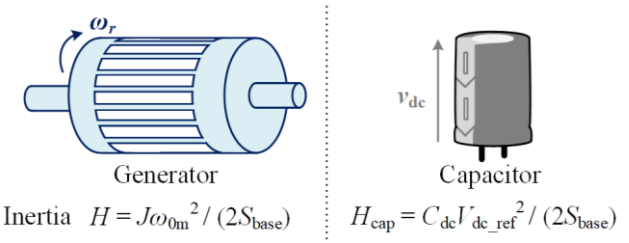

Fig. 1. Inertia mapping between the synchronous generator and the capacitor [29].

energy stored in the rotating masses of the synchronous generator ($J\omega_{0m}^2 / 2$) to its rated power S_{base}, which can be expressed as [4]

$$H = \frac{J\omega_{0m}^2}{2S_{base}}, \quad (1)$$

where J denotes the combined moment of inertia of the synchronous generator and turbine. ω_{0m} stands for the rated rotor mechanical speed. Similarly, the inertia constant of the capacitor H_{cap} can be defined as the ratio of the electrical energy stored in the capacitor ($C_{dc}V_{dc\_ref}^2 / 2$) to its rated power S_{base}, which can be expressed as [29]

$$H_{cap} = \frac{C_{dc}V_{dc\_ref}^2}{2S_{base}}, \quad (2)$$

in which C_{dc} and V_{dc_ref} represent the capacitance and rated capacitor voltage, respectively. The rotor speed ω_r (note that the electrical speed ω_r equals the mechanical speed ω_m for synchronous generators with one pair of poles) and capacitor voltage v_{dc} have the same role in determining the corresponding inertia constant, H and H_{cap}, as noticed in (1) and (2). Therefore, the virtual inertia with an equivalent inertia coefficient of $H_{cap}K_{\omega v\_pu}$ can be expected from the capacitor after the per unit capacitor voltage and the per unit rotor speed or the grid frequency are linked through the proportional gain $K_{\omega v\_pu}$, where [29]

$$\Delta v_{dc\_pu} = K_{\omega v\_pu}\Delta\omega_{r\_pu}. \quad (3)$$

B. Power Converters with Virtual Inertia Control

Fig. 2 shows the schematic diagram of a three-phase grid-connected power converter with the virtual inertia control, where the power grid is modelled as a series connection of an ideal voltage source v_{abc} and a grid inductor L_g. In the case of weak grids (large L_g), the voltage drop across L_g can be considerable, thereby making the measured voltages at the point of common coupling (PCC) v_{gabc} significantly different from the ideal grid voltages v_{abc}. A two-level three-phase power converter with an output inductor filter L_c is employed to investigate the potential instability issue due to inertia emulation. As shown in Fig. 2, the control structure of the system consists of two parts – a virtual inertia controller and a conventional cascaded voltage/current controller implemented in the synchronous dq-frame [29], [30]. The virtual inertia controller is expected to change the DC-link voltage reference by providing a voltage difference Δv_{dc_ref}.

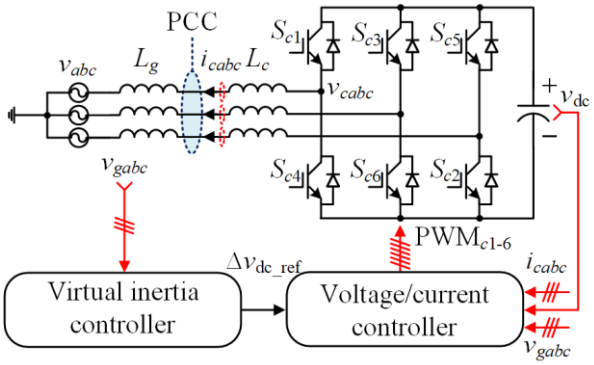

Fig. 2. Schematic diagram of a three-phase grid-connected power converter with the virtual inertia control (PWM stands for pulse-width modulation).

The voltage adjustment by the virtual inertia controller should be proportional to the change of the grid angular frequency $\Delta\omega_r$ in order to generate an appropriate amount of virtual inertia, while the voltage/current controller simply regulates the DC-link voltage v_{dc} to follow the voltage reference adjusted by the virtual inertia controller.

Detailed control schemes will be elaborated in the following sections based on the system and control parameters in Table I. It should be highlighted that the adopted virtual inertia control regulates the DC-link voltage in proportional to the grid frequency for inertia emulation. Therefore, it only needs the frequency signal rather than the df / dt signal, and hence it is different from the df / dt-based scheme. In addition, the adopted virtual inertia control is applied to "grid-following" power converters, which are controlled as AC current sources and cannot operate alone in the islanded mode.

III. Instability under Weak Grid Conditions

This section will detail the control philosophy and explore the instability for the three-phase grid-connected power converters with the virtual inertia control under weak grid conditions.

A. Control without Virtual Inertia

The relationship between the converter voltages v_{cabc} and grid voltages v_{abc} can mathematically be described by the following equation in the synchronous dq-frame [39]:

$$\begin{cases} v_{cd}(t) = v_d(t) + L_t\dfrac{di_{cd}(t)}{dt} - \omega_0 L_t i_{cq}(t) \\ v_{cq}(t) = v_q(t) + L_t\dfrac{di_{cq}(t)}{dt} + \omega_0 L_t i_{cd}(t) \end{cases}, \quad (4)$$

where $v_{cd}(t)$ and $v_{cq}(t)$ denote the d- and q-axis components of converter voltages, $v_d(t)$ and $v_q(t)$ represent the d- and q-axis components of grid voltages, $i_{cd}(t)$ and $i_{cq}(t)$ designate the d- and q-axis components of converter currents, respectively, L_t is the total inductance (i.e., $L_t = L_c + L_g$), and ω_0 stands for the fundamental angular frequency. The terms $-\omega_0 L_t i_{cq}(t)$ and $\omega_0 L_t i_{cd}(t)$ are caused by the cross-coupling effect between the

This article has been accepted for publication in a future issue of this journal, but has not been fully edited. Content may change prior to final publication. Citation information: DOI 10.1109/TPEL.2018.2885513, IEEE Transactions on Power Electronics

Table I. System and control parameter values.

Description	System parameter		Description	Control parameter	
	Symbol	Value		Symbol	Value
DC-link voltage reference	$V_{\text{dc\_ref}}$	400 V	**PLL proportional gain**	$K_{\text{pll\_}p}$	3 (rad/s)/V
Filter inductance	L_c	2 mH	**PLL integral gain**	$K_{\text{pll\_}i}$	300 (rad/s)/(V·s)
Grid inductance	L_g	5 mH	**Current proportional gain**	K_{cp}	15 V/A
DC-link capacitance	C_{dc}	2.82 mF	**Current integral gain**	K_{ci}	300 V/(A·s)
Grid voltage amplitude	V_{d}	155 V	**Voltage proportional gain**	K_{vp}	0.2 A/V
Power rating	S_{base}	1 kVA	**Voltage integral gain**	K_{vi}	2 A/(V·s)
Sampling/switching frequency	f_s / f_{sw}	10 kHz	**Inertia control gain**	$K_{\omega v}$ / $K_{\omega v\_\text{pu}}$	14.32 / 11.25 V/(rad/s)
Frequency reference	f_0	50 Hz	**Time delay constant**	T_d	1.5 / f_s
Generator inertia constant	H	5 s	**Virtual inertia coefficient**	$H_{\text{cap}}K_{\omega v\_\text{pu}}$	2.5 s

d- and *q*-axis. Although the cross-coupling effect due to the filter inductance L_c may be suppressed by the current feedforward control, the effect of the grid inductance L_g can be dominant in a weak grid condition, and this effect is difficult to be predicted and eliminated [1]. To facilitate the analysis, the current feedforward control is not included here. The system in (4) can be expressed in the complex frequency domain as

$$\begin{cases}\left[v_{cd}(s)-v_d(s)+\omega_0 L_t i_{cq}(s)\right]G_{\text{plant}}(s)=i_{cd}(s)\\ \left[v_{cq}(s)-v_q(s)-\omega_0 L_t i_{cd}(s)\right]G_{\text{plant}}(s)=i_{cq}(s)\end{cases}, \tag{5}$$

where $G_{\text{plant}}(s)$ can be represented by

$$G_{\text{plant}}(s)=\frac{1}{L_t s}. \tag{6}$$

Proportional integral (PI) controllers are employed as the current controller $G_i(s)$ and voltage controller $G_v(s)$, expressed as

$$G_i(s)=K_{cp}+\frac{K_{ci}}{s}, \tag{7}$$

$$G_v(s)=-(K_{vp}+\frac{K_{vi}}{s}), \tag{8}$$

where the minus sign is caused by the definition of converter current directions in Fig. 2. Considering the time-delay introduced by reference computations and pulse updates, whose effect can be simplified as a first-order lag to approximately model its low-frequency characteristics for simplicity [38]:

$$G_d(s)=\frac{1}{T_d s+1}, \tag{9}$$

in which T_d = 1.5 / f_s with f_s being the sampling frequency, the control architecture of the cascaded voltage/current controller is shown in Fig. 3. It is clear from Fig. 3(a) that the DC-link voltage v_{dc} is regulated to its reference $v_{\text{dc\_ref}}$ (normally it is a constant $V_{\text{dc\_ref}}$) through the control of the *d*-axis current i_{cd}. Variations in the *d*-axis current i_{cd} will directly affect v_{dc} through a transfer function $G_{iv}(s)$, which is caused by the real-time power balance between the AC-side and DC-side of the three-phase power converter. Under the assumption of an ideal lossless conversion, it can be derived as

$$G_{iv}(s)=\frac{-3V_d}{2V_{\text{dc\_ref}}C_{\text{dc}}s}, \tag{10}$$

where V_d denotes the rated value of v_d and $V_{\text{dc\_ref}}$ stands for the reference value of v_{dc}. The grid synchronization can be achieved using a PLL. It enables the detection of the phase-angle from the PCC voltages v_{gabc}. According to [38] and [39], the PLL will influence both the *d*- and *q*-axis current control due to the transformations between natural frame and synchronous frame. When the grid-connected power converter is operated with a unity power factor, the influence of the PLL on the converter control is reflected in the *q*-axis. As shown in Fig. 3(b), the extra terms $I_{cd}\Delta\theta_{\text{pll}}$ and $V_d\Delta\theta_{\text{pll}}$ are introduced by the PLL. I_{cd} denotes the rated value of i_{cd}, and $\Delta\theta_{\text{pll}}$ represents the difference between the phase-angle locked by the PLL and that of PCC voltages. Although the

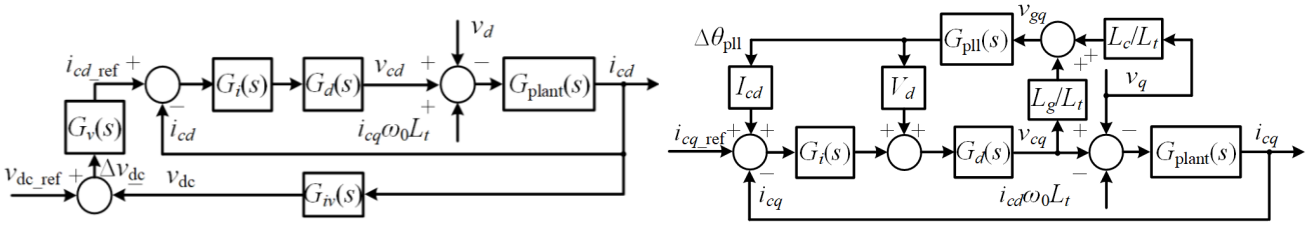

(a) Control in *d*-axis (b) Control in *q*-axis

Fig. 3. Voltage/current controller implemented in the synchronous reference frame.

This article has been accepted for publication in a future issue of this journal, but has not been fully edited. Content may change prior to final publication. Citation information: DOI 10.1109/TPEL.2018.2885513, IEEE Transactions on Power Electronics

PLL is assumed to only affect the *q*-axis current control, it should be noted that the *d*-axis current i_{cd} will influence the PLL (e.g., its phase angle $\Delta\theta_{\text{pll}}$) through the coupling between *d*-axis and *q*-axis, and this effect will be analyzed in the following sections.

A small-signal model of the PLL is given in Fig. 4, from which the relationship between $\Delta\theta_{\text{pll}}$ and v_{gq} can be derived and represented as [38]

$$G_{\text{pll}}(s)=\frac{\Delta\theta_{\text{pll}}(s)}{v_{gq}(s)}=\frac{K_{\text{pll\_}p}s+K_{\text{pll\_}i}}{s^2+V_dK_{\text{pll\_}p}s+V_dK_{\text{pll\_}i}}. \quad (11)$$

where $K_{\text{pll\_}p}$ and $K_{\text{pll\_}i}$ denote the proportional and integral gains of the PLL loop filter (i.e., a PI controller), respectively. Detailed derivations of the PLL model and its influence on the current control are elaborated in [38] and [39]. It is revealed that the PLL proportional gain K_p rather than the PLL integral gain K_i will play a dominant role in determining the system stability [39]. An excessively large K_p will destabilize the power converter control under weak grids. In contrast, an excessively small K_p will deteriorate the PLL dynamics. In this paper, $K_{\text{pll\_}p}$ and $K_{\text{pll\_}i}$ are designed to yield a crossover frequency of 75 Hz and a phase margin of 75˚ for the PLL control. This design guarantees the stable operation of power converters without the virtual inertia control as well as fair PLL dynamics.

The closed-loop transfer functions of the *d*- and *q*-axis current control $G_{id\_\text{cl}}(s)$ and $G_{iq\_\text{cl}}(s)$ can be derived from Fig. 3 as

$$G_{id\_\text{cl}}(s)=\frac{i_{cd}(s)}{i_{cd\_\text{ref}}(s)}=\frac{G_i(s)G_d(s)G_{\text{plant}}(s)}{1+G_i(s)G_d(s)G_{\text{plant}}(s)}, \quad (12)$$

$$G_{iq\_\text{cl}}(s)=\frac{i_{cq}(s)}{i_{cq\_\text{ref}}(s)}=\frac{L_tG_i(s)G_d(s)G_{\text{plant}}(s)}{L_t-L_gG_d(s)G_{\text{pll}}(s)\left[I_{cd}G_i(s)+V_d\right]+L_tG_i(s)G_d(s)G_{\text{plant}}(s)}. \quad (13)$$

Furthermore, the voltage-loop gain without the virtual inertia control $G_{v\_\text{ol\_wo}}(s)$ is derived as

$$G_{v\_\text{ol\_wo}}(s)=\frac{v_{\text{dc}}(s)}{\Delta v_{\text{dc}}(s)}=G_v(s)G_{id\_\text{cl}}(s)G_{iv}(s). \quad (14)$$

Moreover, the closed-loop transfer function of the voltage control without the virtual inertia control $G_{v\_\text{cl\_wo}}(s)$ can be represented as a function of $G_{v\_\text{ol\_wo}}(s)$ as

$$G_{v\_\text{cl\_wo}}(s)=\frac{v_{\text{dc}}(s)}{v_{\text{dc\_ref}}(s)}=\frac{G_{v\_\text{ol\_wo}}(s)}{1+G_{v\_\text{ol\_wo}}(s)}. \quad (15)$$

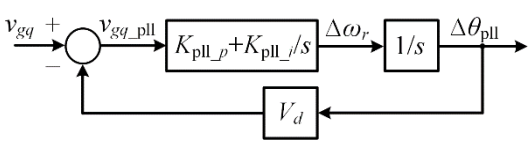

Fig. 4. A linear small-signal model of the PLL.

Fig. 5 illustrates the Bode diagram of the voltage-loop gain without the virtual inertia control $G_{v\_\text{ol\_wo}}(s)$, where a positive gain margin of 44 dB can readily be obtained, indicating a large stability margin. Fig. 6 illustrates the pole-zero map of the closed-loop transfer function of the voltage control without the virtual inertia control $G_{v\_\text{cl\_wo}}(s)$, and the corresponding zoom-in inset is also provided. Since all the closed-loop poles are in the left-half-plane, the voltage and current control under weak grid conditions can always be stable with the parameter values listed in Table I.

B. Control with Virtual Inertia

Referring back to Fig. 3(b), because of the coupling effect between the *d*- and *q*-axis, variations of i_{cd} will change $\Delta\theta_{\text{pll}}$. Considering the coupling effect, it is possible to derive the transfer function from i_{cd} to $\Delta\theta_{\text{pll}}$, i.e., $G_{id\_\Delta\theta}(s)$, as

$$G_{id\_\Delta\theta}(s)=\frac{\Delta\theta_{\text{pll}}(s)}{i_{cd}(s)}=\omega_0L_gG_{iq\_\text{cl}}(s)G_{\text{pll}}(s). \quad (16)$$

The Bode diagram of $G_{id\_\Delta\theta}(s)$ is illustrated in Fig. 7. It is obvious that $G_{id\_\Delta\theta}(s)$ exhibits a low-pass filter characteristic. As compared to that of i_{cd}, the magnitude of $\Delta\theta_{\text{pll}}$ has been

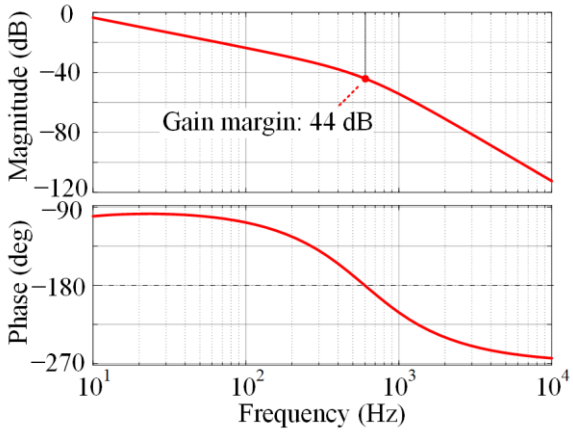

Fig. 5. Bode diagram of the voltage-loop gain without the virtual inertia control $G_{v\_\text{ol\_wo}}(s)$.

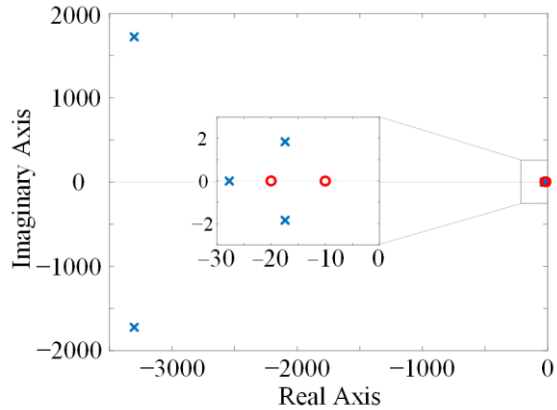

Fig. 6. Pole-zero map of the closed-loop transfer function of the voltage control without the virtual inertia control $G_{v\_\text{cl\_wo}}(s)$.

This article has been accepted for publication in a future issue of this journal, but has not been fully edited. Content may change prior to final publication. Citation information: DOI 10.1109/TPEL.2018.2885513, IEEE Transactions on Power Electronics

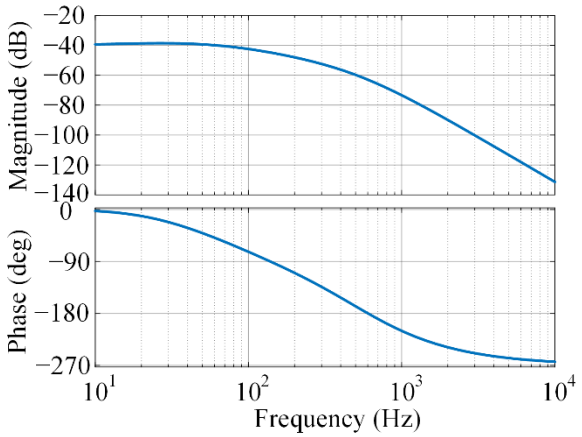

Fig. 7. Bode diagram of $G_{id\_\Delta\theta}(s)$, i.e., the transfer function from i_{cd} to $\Delta\theta_{\text{pll}}$.

attenuated more than −40 dB. This is because the PLL transfer function $G_{\text{pll}}(s)$ can be approximated to a gain $(1 / V_d)$ in the low frequency band according to (11), and V_d is greater than 100 V here. As a result, the *d*-axis current control has almost no effect on the PLL, and thus the coupling effect between the two axes are often ignored when analysing the instability issue due to PLLs for simplicity [39].

By directly linking the change of the capacitor voltage reference $\Delta v_{\text{dc\_ref}}$ and the change of the grid angular frequency $\Delta\omega_r$ through a proportional gain $K_{\omega v}$, virtual inertia can be provided by the three-phase grid-connected converter [29]. It should be emphasized that $\Delta\omega_r$ is normally obtained from the PLL in practice. Mathematically, $\Delta\omega_r$ equals the time-derivative of the phase-angle $\Delta\theta_{\text{pll}}$, i.e., $\Delta\omega_r = \Delta\theta_{\text{pll}}s$, as can be observed from Fig. 4. Therefore, the virtual inertia control inherently introduces a differential operator between $\Delta\theta_{\text{pll}}$ and $\Delta v_{\text{dc\_ref}}$, as shown in Fig. 8, where the entire control structure for the three-phase power converter with the virtual inertia control is given. Note that $\Delta\omega_r$ is expressed as the time derivative of $\Delta\theta_{\text{pll}}$ in Fig. 8, while $\Delta\theta_{\text{pll}}$ is represented as the integral of $\Delta\omega_r$ in Fig. 4. In fact, these two representations are equivalent.

According to Fig. 8, the transfer function from i_{cd} to $\Delta v_{\text{dc\_ref}}$, denoted as $G_{id\_\Delta\text{vref}}(s)$, is given by

$$G_{id\_\Delta\text{vref}}(s) = \frac{\Delta v_{\text{dc\_ref}}(s)}{i_{cd}(s)} = G_{id\_\Delta\theta}(s)K_{\omega v}s. \tag{17}$$

Although the differential operator in (17) inserted between $\Delta\omega_r$ and $\Delta\theta_{\text{pll}}$ is quite necessary for inertia emulation, it also makes $\Delta v_{\text{dc\_ref}}$ very sensitive to i_{cd}, particularly for a large value of $K_{\omega v}$, as evidenced by the magnitude diagram of $G_{id\_\Delta\text{vref}}(s)$ shown in Fig. 9, which serves to illustrate the effect of the virtual inertia control. The mechanism for magnitude amplification can be explained by the transfer function $G_{\text{pll}\_\omega r}(s)$, namely $\Delta\omega_r(s) / v_{gq}(s)$, which is essentially the multiplication of the PLL transfer function in (11) and the differential operator *s*:

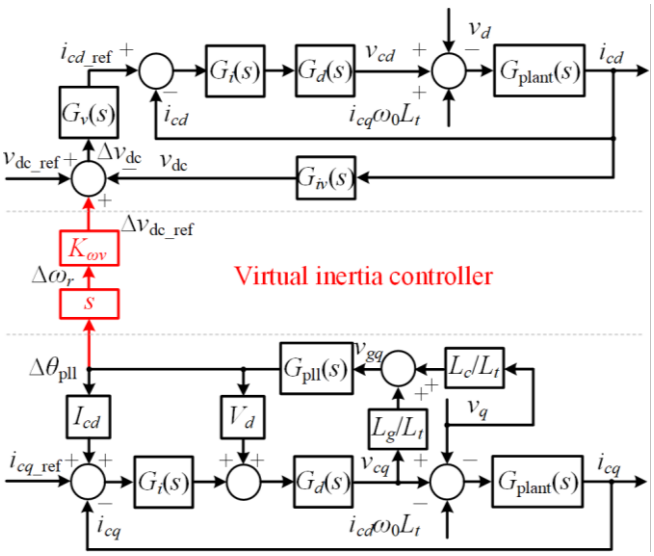

Fig. 8. Entire control structure for the three-phase power converter with the virtual inertia control.

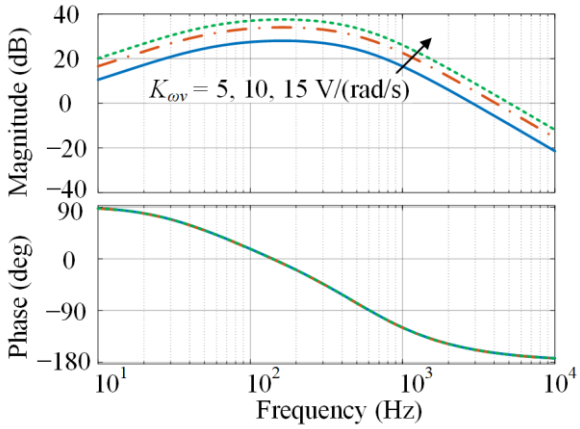

Fig. 9. Bode diagram of $G_{id\_\Delta\text{vref}}(s)$, i.e., the transfer function from i_{cd} to $\Delta v_{\text{dc\_ref}}$ with the conventional virtual inertia control.

$$G_{\text{pll}\_\omega r}(s) = \frac{K_{\text{pll}\_p}s^2 + K_{\text{pll}\_i}s}{s^2 + V_d K_{\text{pll}\_p}s + V_d K_{\text{pll}\_i}}. \tag{18}$$

As compared to (11), the differential operator reshapes the PLL transfer function from a low-pass filter $G_{\text{pll}}(s)$ to a high-pass filter $G_{\text{pll}\_\omega r}(s)$. In addition, $G_{\text{pll}\_\omega r}(s)$ can be approximated as a gain of K_{pll_p} in the high-frequency band. Since $K_{\text{pll}\_p} > 1$ (rad/s)/V, the magnitude will be amplified by the differential operator. The effect of magnitude amplification, together with the considerable phase-shift of $G_{id\_\Delta\text{vref}}(s)$, tends to destabilize the power conversion system, and the instability issue will be disclosed as follows.

It can be obtained from Fig. 8 that the branch from i_{cd} to $\Delta v_{\text{dc\_ref}}$ is in parallel with the branch from i_{cd} to v_{dc}. First, note that one branch links i_{cd} to v_{dc} through $G_{iv}(s)$. Additionally, the other branch starts from the term $i_{cd}\omega_0 L_t$ (i.e., i_{cd} multiplied by $\omega_0 L_t$), goes through the *q*-axis current control

This article has been accepted for publication in a future issue of this journal, but has not been fully edited. Content may change prior to final publication. Citation information: DOI 10.1109/TPEL.2018.2885513, IEEE Transactions on Power Electronics

to $\Delta\theta_{\text{pll}}$, and finally reaches $\Delta v_{\text{dc\_ref}}$ through the multiplication of $K_{\omega v}$ and s. Since the inputs of the two branches (namely i_{cd}) are the same, and the corresponding outputs are operated in the same summing node, the two branches are in parallel. The additional branch from i_{cd} to $\Delta v_{\text{dc\_ref}}$ essentially models the effect of the virtual inertia control, which may cause the instability issue, as will be detailed. Substitution of (16) into (17), it is noted that the gain of this additional branch is determined by the grid inductance L_g. If L_g = 0 mH, the additional branch will be disabled. Therefore, the instability issue will not occur under stiff grids where L_g = 0 mH. In addition, the increase of L_g will intensify the influence of the virtual inertia control on the system stability. Since the two branches are in parallel, they can be combined with $\Delta v_{\text{dc\_ref}}$ being regarded as a part of v_{dc}. In this sense, ($v_{\text{dc}} - \Delta v_{\text{dc\_ref}}$) will be the output of the modified voltage-loop in replacement of v_{dc}. The loop-gain of the modified voltage-loop with the conventional virtual inertia control $G_{v\_\text{ol\_wc}}(s)$ can be derived as

$$\begin{aligned} G_{v\_\text{ol\_wc}}(s) &= \frac{v_{\text{dc}}(s) - \Delta v_{\text{dc\_ref}}(s)}{\Delta v_{\text{dc}}(s)} \\ &= G_v(s)G_{id\_\text{cl}}(s)\left[G_{iv}(s) - G_{id\_\Delta\text{vref}}(s)\right]. \end{aligned} \tag{19}$$

The Bode diagram of $G_{v\_\text{ol\_wc}}(s)$ is drawn in Fig. 10, where the negative phase margins and gain margins clearly demonstrate the instability of the voltage control. Moreover, the similarities between the magnitude curves of Fig. 9 and Fig. 10 indicate that $G_{id\_\Delta\text{vref}}(s)$ may greatly influence the voltage control because of its magnitude amplification effect. To further verify the instability of the voltage control, the closed-loop transfer function of the voltage control with the conventional virtual inertia control $G_{v\_\text{cl\_wc}}(s)$ is derived as

$$\begin{aligned} G_{v\_\text{cl\_wc}}(s) &= \frac{v_{\text{dc}}(s)}{v_{\text{dc\_ref}}(s)} \\ &= \frac{G_v(s)G_{id\_\text{cl}}(s)G_{iv}(s)}{1 - G_v(s)G_{id\_\text{cl}}(s)G_{id\_\Delta\text{vref}}(s) + G_v(s)G_{id\_\text{cl}}(s)G_{iv}(s)}. \end{aligned} \tag{20}$$

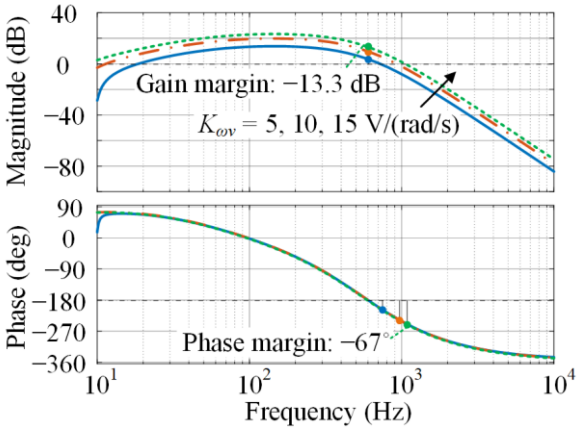

Fig. 10. Bode diagram of the voltage-loop gain with the conventional virtual inertia control $G_{v\_\text{ol\_wc}}(s)$.

Substituting of (14) into (15) and then comparing (15) with (20), it is noted that an additional term $-G_v(s)G_{id\_\text{cl}}(s)G_{id\_\Delta\text{vref}}(s)$ is added to the denominator of $G_{v\_\text{cl\_wc}}(s)$, and this term causes the instability of the voltage control.

Fig. 11 presents the pole-zero map of the voltage control with the conventional virtual inertia control, where a gain $K_{\omega v}$ of 14.32 is used and henceforth, as given in Table I. As observed, a pair of conjugate poles appearing in the right-half plane (RHP) will make the voltage control unstable, which is consistent with Fig. 10. Although the presented stability analysis is on the basis of a single closed-loop transfer function of the voltage control, it essentially describes the relationship between the most concerned input and output of practical multiple input multiple output power conversion systems.

IV. Proposed Modified Virtual Inertia Control for Stability Enhancement

According to the previous analysis, the magnitude amplification of the differential operator should be responsible for the system instability. In this section, the differential operator is intentionally modified in order to reduce its high-frequency amplification effect, and thus to improve the system stability.

As mentioned before, $G_{\text{pll\_}\omega r}(s)$ can be simplified into $K_{\text{pll\_}p}$ in the high-frequency band. This is because of the second-order term ($K_{\text{pll\_}p}s^2$) in the numerator of $G_{\text{pll\_}\omega r}(s)$ in (18). The proposed control scheme aims to reduce the coefficient of this second-order term. Its fundamental principle is shown in Fig. 12, where the change of the modified angular frequency $\Delta\omega_m$ will be used instead of $\Delta\omega_r$ to generate $\Delta v_{\text{dc\_ref}}$ through the proportional gain $K_{\omega v}$. The transfer function $G_{\text{pll\_}\omega m}(s)$ from v_{gq} to $\Delta\omega_m$ can be derived from Fig. 12(a) as

$$G_{\text{pll\_}\omega m}(s) = \frac{(K_{\text{pll\_}p} - K_m)s^2 + K_{\text{pll\_}i}s}{s^2 + V_d K_{\text{pll\_}p}s + V_d K_{\text{pll\_}i}}, \tag{21}$$

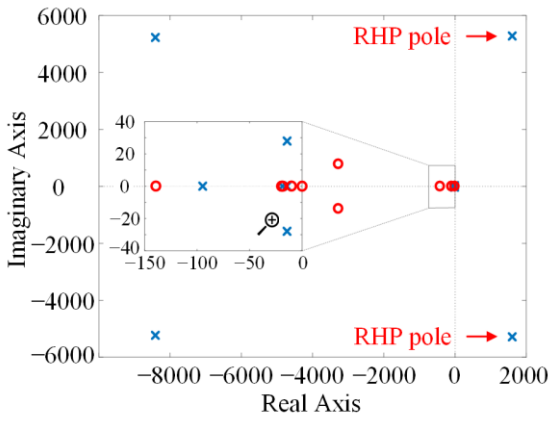

Fig. 11. Pole-zero map of the closed-loop transfer function of the voltage control with the conventional virtual inertia control $G_{v\_\text{cl\_wc}}(s)$.

This article has been accepted for publication in a future issue of this journal, but has not been fully edited. Content may change prior to final publication. Citation information: DOI 10.1109/TPEL.2018.2885513, IEEE Transactions on Power Electronics

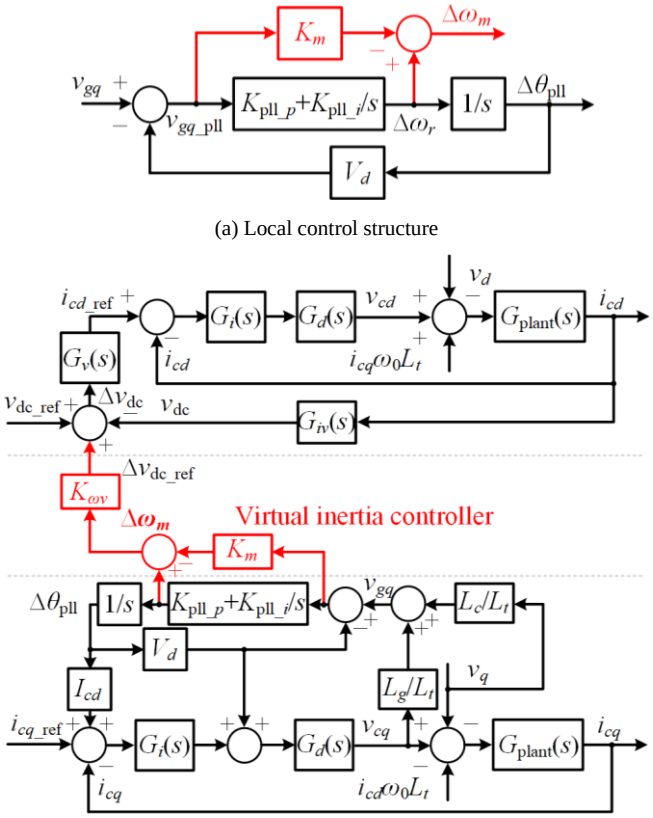

(a) Local control structure

(b) Overall control structure

Fig. 12. Fundamental principle of the proposed control scheme.

where K_m denotes the proportional gain of the proposed modified virtual inertia control. Notice that this control scheme will not affect the frequency detection when the PLL locks the grid voltage, since $v_{gq\_pll} = 0$ in steady state. By comparing $G_{pll\_\omega r}(s)$ in (18) and $G_{pll\_\omega m}(s)$, it is noted that the proposed control scheme essentially attaches the following transfer function to the differential operator:

$$G_m(s) = \frac{G_{pll\_\omega m}(s)}{G_{pll\_\omega r}(s)} = \frac{(K_{pll\_p} - K_m)s + K_{pll\_i}}{K_{pll\_p}s + K_{pll\_i}}, \quad (22)$$

where $G_m(s)$ would be a lead-lag compensator when $K_m \neq K_{pll\_p}$ or a low-pass filter if $K_m = K_{pll\_p}$. Considering (22), the transfer function from i_{cd} to Δv_{dc_ref} should be reorganized as $G_{id\_\Delta vref\_wp}(s)$:

$$G_{id\_\Delta vref\_wp}(s) = \frac{\Delta v_{dc\_ref}(s)}{i_{cd}(s)} = G_{id\_\Delta\theta}(s)G_m(s)K_{\omega v}s. \quad (23)$$

The Bode diagram of $G_{id\_\Delta vref\_wp}(s)$ is plotted in Fig. 13. As K_m increases and approaches K_{pll_p} ($K_m \neq K_{pll\_p}$), the magnitude of $G_{id\_\Delta vref\_wp}(s)$ drops without any compromise on the phase-shift, particularly in the high-frequency band which is more of concern. When K_m reaches K_{pll_p} ($K_m = K_{pll\_p}$), the dramatic attenuation of the magnitude of $G_{id\_\Delta vref\_wp}(s)$ can be achieved at the expense of an additional 90-degree phase lag. Referring to (22), this additional phase lag is caused by the degradation of the numerator order of $G_m(s)$ when $K_m = K_{pll\_p}$. Regardless of phase-shifts, the proposed control scheme

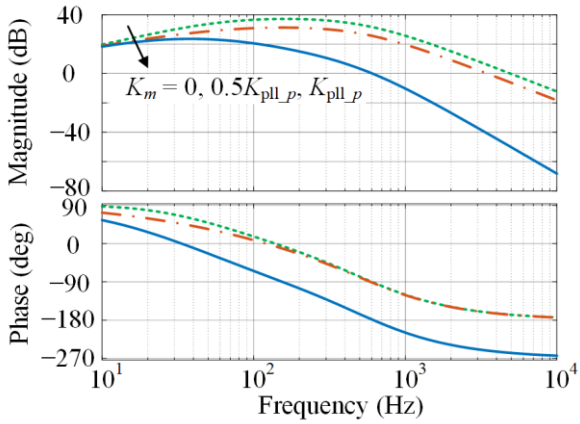

Fig. 13. Bode diagram of $G_{id\_\Delta vref\_wp}(s)$, i.e., the transfer function from i_{cd} to Δv_{dc_ref} with the proposed virtual inertia control.

manages to attenuate the magnitude amplification, and this result can be beneficial in terms of system stability.

Furthermore, the loop-gain of the modified voltage-loop with the proposed virtual inertia control $G_{v\_ol\_wp}(s)$ is written as

$$G_{v\_ol\_wp}(s) = \frac{v_{dc}(s) - \Delta v_{dc\_ref}(s)}{\Delta v_{dc}(s)} = G_v(s)G_{id\_cl}(s)\left[G_{iv}(s) - G_{id\_\Delta vref\_wp}(s)\right]. \quad (24)$$

Fig. 14 illustrates the Bode diagram of the voltage-loop gain with the proposed virtual inertia control $G_{v\_ol\_wp}(s)$, where the stability enhancement can clearly be observed. When $K_m = 0.5K_{pll\_p}$, although the system featuring a negative phase margin and a negative gain margin is unstable, both margins are improved. The case of $K_m = K_{pll\_p}$ results in a system with a gain margin of 4.35 dB and a phase margin of 34.1 degrees, and these positive stability indices indicate the system is stable.

The closed-loop transfer function of the voltage control with the proposed virtual inertia control $G_{v\_cl\_wp}(s)$ is derived as

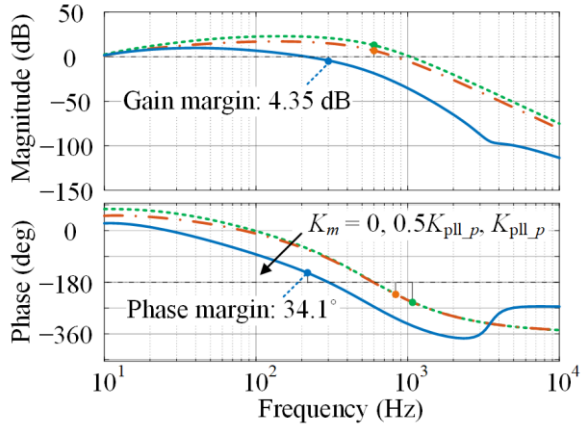

Fig. 14. Bode diagram of the voltage-loop gain with the proposed virtual inertia control $G_{v\_ol\_wp}(s)$.

This article has been accepted for publication in a future issue of this journal, but has not been fully edited. Content may change prior to final publication. Citation information: DOI 10.1109/TPEL.2018.2885513, IEEE Transactions on Power Electronics

$$G_{v\_cl\_wp}(s)=\frac{v_{dc}(s)}{v_{dc\_ref}(s)} =\frac{G_v(s)G_{id\_cl}(s)G_{iv}(s)}{1-G_v(s)G_{id\_cl}(s)G_{id\_\Delta vref\_wp}(s)+G_v(s)G_{id\_cl}(s)G_{iv}(s)}. \quad (25)$$

The Pole-zero map of $G_{v\_cl\_wp}(s)$ is further provided in Fig. 15. Note that all the closed-loop poles of the voltage control are located in the left-half-plane, thereby demonstrating a stable system. It should be commented that as long as the pole of $G_m(s)$ locates leftwards to its zero, i.e., $|K_{pll\_p}-K_m|<K_{pll\_p}$, the proposed control scheme will enable magnitude attenuation and consequently, the stability is improved.

V. Experimental Verifications

The instability issue of the three-phase grid-connected converters with the virtual inertia control will further be experimentally investigated in this section. Moreover, the effectiveness of the proposed modified virtual inertia control in addressing the instability issue will also be verified. In the experiments, the grid voltages v_{abc} were formed by a virtual synchronous generator (VSG), which is essentially a three-phase power converter exhibiting the same electrical terminal characteristics as conventional synchronous generators, providing the base power system inertia and forming the grid voltages [40]. The reason for the employment of the VSG lies in the replacement of conventional synchronous generators and proper regulation of the grid frequency so as to demonstrate the benefits of virtual inertia. A step-by-step design of the VSG control, together with its design parameters, can be found in [29] and [41]. In addition to the VSG, other parts of the system with the parameters listed in Table I are shown schematically in Fig. 2. Control systems were implemented in a dSPACE control platform (Microlabbox). An eight-channel oscilloscope (TELEDYNE LECROY: HDO8038) was used to capture all the experimental waveforms.

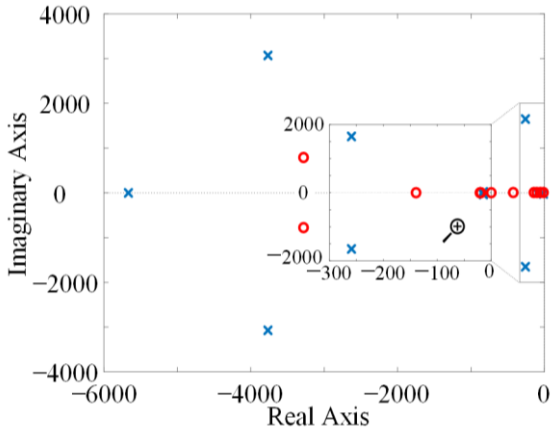

Fig. 15. Pole-zero map of the closed-loop transfer function of the voltage control with the proposed virtual inertia control $G_{v\_cl\_wp}(s)$.

Fig. 16 presents the steady-state experimental results of the three-phase power converter with the conventional virtual inertia control, where Δf_r ($\Delta\omega_r = 2\pi\Delta f_r$) denotes the grid frequency change measured by the PLL, and the other notations can be found in Fig. 2. In this case, the VSG is employed solely to provide the grid voltages with a fixed frequency as an AC voltage source. As observed, the current waveforms i_{cabc} are seriously distorted. It should be mentioned that the saturation units are necessary in practice to limit the variation ranges of the DC-link voltage v_{dc} and frequency f_r to avoid over voltages. Due to the saturation units, v_{dc} and f_r can only oscillate within certain ranges rather than being completely unstable. Therefore, the oscillations in the grid frequency change Δf_r imply that the virtual inertia control through the direct link between f_r and v_{dc} should be responsible for the instability. Fortunately, the instability issue can successfully be addressed once the proposed modified virtual inertia control is enabled, as demonstrated in Fig. 17. It is clear that the oscillations in the grid frequency change Δf_r and the DC-link voltage v_{dc} disappear. Due to the stable DC-link voltage v_{dc}, the converter currents become almost distortion-free with negligible variations (induced by power converter losses). These experimental results agree well with the pole-zero maps shown in Fig. 11 and Fig. 15. It should be noted that the instability due to the virtual inertia control remains even if the PLL is replaced by other more

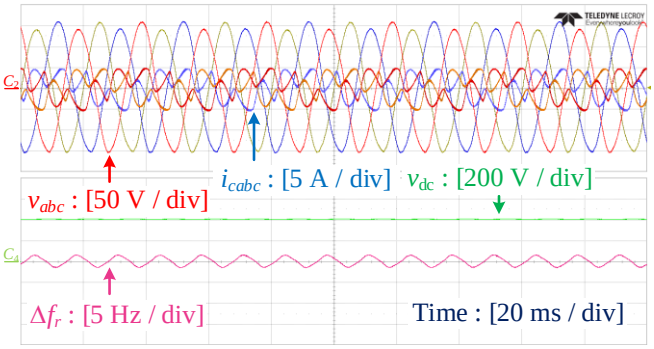

Fig. 16. Steady-state experimental results of the power converter with the conventional virtual inertia control (v_{abc}: the grid voltages, i_{cabc}: the converter currents, v_{dc}: the DC-link voltage, and Δf_r: the frequency change).

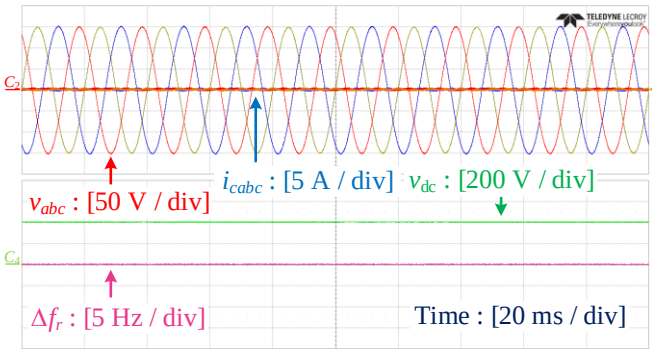

Fig. 17. Steady-state experimental results of the power converter with the proposed virtual inertia control (v_{abc}: the grid voltages, i_{cabc}: the converter currents, v_{dc}: the DC-link voltage, and Δf_r: the frequency change).

This article has been accepted for publication in a future issue of this journal, but has not been fully edited. Content may change prior to final publication. Citation information: DOI 10.1109/TPEL.2018.2885513, IEEE Transactions on Power Electronics

robust synchronization units, such as the frequency-locked-loop (FLL) [21], or with modified PLL designs.

Through the proposed virtual inertia control, the three-phase grid-connected power converter may effectively contribute virtual inertia to weak power grids. For illustration, Fig. 18 shows the grid frequency and the DC-link voltage responses of the power converters with and without the virtual inertia control when they experienced a 5% step-up load change. Such a step-up load change causes a relatively serious frequency event, which is sometimes used to emulate generation or load tripping in real power systems [5], [42]. It should be mentioned that the step-up load change causes the demanded power to be greater than the generated power. As a consequence, the grid frequency drops, which is seen by all the synchronous generators as a common signal to increase their respective power outputs for balancing the power mismatch between generation and demand. In the case of such a frequency event, it is important to keep the frequency drop, as well as its changing rate, i.e., the rate of change of frequency (RoCoF), below the limits defined by grid codes [3]. Otherwise, excessive frequency drops may further cause generation and load tripping, thus leading to cascaded failures. In extreme cases, system blackouts may even occur [4].

In Fig. 18, the VSG is operated to regulate the grid frequency in a similar way as conventional synchronous generators do. As compared to the grid-connected power converter without the virtual inertia control, the power converter with the virtual inertia control registers a change of its DC-link voltage that is proportional to the grid frequency for inertia emulation during the frequency event. As a result, the inertia constant is improved from 5 s to 7.5 s, indicating a 50% enhancement of the power system inertia. The increased inertia can contribute to an 11% increment of the frequency nadir (i.e., the lowest frequency point) and a 33% improvement of the RoCoF, as demonstrated in Fig. 18. Note that the extent of performance improvements depends on the emulated virtual inertia, which is further determined by the DC-link voltage, voltage variation range, and DC-link capacitance, as detailed in [29].

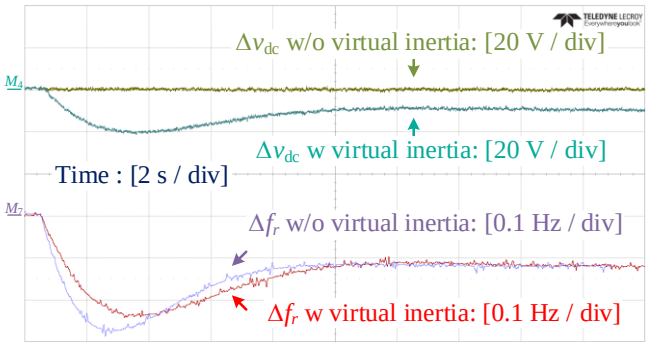

Fig. 18. Experimental results of the power converters with/without the proposed virtual inertia control under a 5% step-up load change (Δv_{dc}: the DC-link voltage change and Δf_r: the frequency change).

VI. Conclusion

This paper has identified the potential instability issue for three-phase grid-connected power converters with the virtual inertia control when they are connected to weak power grids. The exploration indicates that the virtual inertia control introduces an extra link between the *d*-axis current and the DC-link voltage reference through the *d*- and *q*-axis coupling, *q*-axis current control, phase-locked-loop, and virtual inertia controller. Specifically, there is an inherent differential operator inside the link, which is responsible for the instability, when the converter is connected to weak grids. Accordingly, the virtual inertia control has been intentionally modified in order to mitigate the amplification effect introduced by the differential operator. As a result, three-phase grid-connected power converters can effectively contribute virtual inertia to weak power grids, which have been verified by the experimental results. The major contributions of this paper can be summarized as follows:

(1) Identify the instability issue faced by three-phase grid-connected power converters with the virtual inertia control under weak grids;

(2) Explain the mechanism for the instability issue;

(3) Propose a modified virtual inertia control scheme to resolve the instability issue.

References

[1] F. Blaabjerg, R. Teodorescu, M. Liserre, and A. V. Timbus, "Overview of control and grid synchronization for distributed power generation systems," *IEEE Trans. Ind. Electron.*, vol. 53, no. 5, pp. 1398–1409, Oct. 2006.

[2] X. Wang and F. Blaabjerg, "Harmonic stability in power electronic based power systems: concept, modeling, and analysis," *IEEE Trans. Smart Grid*, in press.

[3] International review of frequency control adaptation, Australia Energy Market Operator. Melbourne, VIC, Australia, 2017. [Online]. Available: http://www.aemo.com.au.

[4] P. Kundur, *Power System Stability and Control*. New York, NY, USA: McGraw-Hill, 1994.

[5] G. Delille, B. Francois, and G. Malarange, "Dynamic frequency control support by energy storage to reduce the impact of wind and solar generation on isolated power system's inertia," *IEEE Trans. Sustain. Energy*, vol. 3, no. 4, pp. 931–939, Oct. 2012.

[6] J. M. Carrasco, L. G. Franquelo, J. T. Bialasiewicz, E. Galvan, R. C. P. Guisado, M. A. M. Prats, J. I. Leon, and N. Moreno-Alfonso, "Power electronic systems for the grid integration of renewable energy sources: a survey," *IEEE Trans. Ind. Electron.*, vol. 53, no. 4, pp. 1002–1016, Aug. 2006.

[7] A. F. Hoke, M. Shirazi, S. Chakraborty, E. Muljadi, and D. Maksimovic, "Rapid active power control of photovoltaic systems for grid frequency support," *IEEE J. Emerg. Sel. Topics Power Electron.*, vol. 5, no. 3, pp. 1154–1163, Sep. 2017.

[8] F. Blaabjerg, Y. Yang, D. Yang, and X. Wang, "Distributed power-generation systems and protection," *Proc. IEEE*, vol. 105, pp. 1311-1331, Jul. 2017.

[9] Y. Liu, S. You, J. Tan, Y. Zhang, and Y. Liu, "Frequency response assessment and enhancement of the U.S. power grids towards extra-high photovoltaic generation penetrations – an industry perspective," *IEEE Trans. Power Sys.*, vol. 33, no. 3, pp. 3438–3449, Jan. 2018.

[10] RoCoF Modification Proposal – TSOs' Recommendations, EirGrid/SONI, Ballsbridge, DUB, Ireland, Sep. 4, 2012.

[11] E. Spahic, D. Varma, G. Beck, G. Kuhn, and V. Hild, "Impact of reduced system inertia on stable power system operation and an overview of possible solutions", in *Proc. PESGM*, Boston, MA, USA, 17–21 Jul. 2016.

[12] Z. Chen, J. M. Guerrero, and F. Blaabjerg, "A review of the state of the art of power electronics for wind turbines," *IEEE Trans. Power Electron.*, vol. 24, no. 8, pp. 1859–1875, Aug. 2009.

[13] J. Morren, S. W. H. de Haan, W. L. Kling, and J. A. Ferreira, "Wind turbines emulating inertia and supporting primary frequency control," *IEEE Trans. Power Sys.*, vol. 21, no. 1, pp. 433–434, Feb. 2006.

[14] L. Holdsworth, J. Ekanayake, and N. Jenkins, "Power system frequency response from fixed speed and doubly fed induction generator based wind turbines," *Wind Energy*, vol. 7, pp. 21–35, 2004.

[15] A. Mullane and M. O'Malley, "The inertial response of induction-machine-based wind turbines," *IEEE Trans. Power Sys.*, vol. 20, no. 3, pp. 1496–1503, Aug. 2005.

[16] J. Ekanayake, and N. Jenkins, "Comparison of the response of doubly fed and fixed-speed induction generator wind turbines to changes in network frequency," *IEEE Trans. Energy Conv.*, vol. 19, no. 4, pp. 800−802, Dec. 2004.

[17] G. Lalor, A. Mullane, and M. O'Malley, "Frequency control and wind turbine technologies," *IEEE Trans. Power Sys.*, vol. 20, no. 4, pp. 1905–1913, Nov. 2005.

[18] J. Morren, S. W. H. de Haan, W. L. Kling, and J. A. Ferreira, "Wind turbines emulating inertia and supporting primary frequency control," *IEEE Trans. Power Sys.*, vol. 21, no. 1, pp. 433–434, Feb. 2006.

[19] M. Kayikçi and J. V. Milanovic, "Dynamic contribution of DFIG-based wind plants to system frequency disturbances," *IEEE Trans. Power Sys.*, vol. 24, no. 2, pp. 859–867, May 2009.

[20] I. Serban and C. Marinescu, "Control strategy of three-phase battery energy storage systems for frequency support in microgrids and with uninterrupted supply of local loads," *IEEE Trans. Power Electron.*, vol. 29, no. 9, pp. 5010–5020, Sep. 2014.

[21] J. Fang, R. Zhang, H. Li, and Y. Tang, "Frequency derivative-based inertia enhancement by grid-connected power converters with a frequency-locked-loop," *IEEE Trans. Smart Grid*, in press.

[22] T. Kerdphol, F. S. Rahman, Y. Mitani, M. Watanabe, and S. Kufeoglu, "Robust virtual inertia control of an islanded microgrid considering high penetration of renewable energy," *IEEE Access*, vol. 6, pp. 625-636, Feb. 2018.

[23] D. Duckwitz, M. Shan, and B. Fischer, "Synchronous inertia control for wind turbines—Adaption of the virtual synchronous machine to wind turbines for providing distributed contributions to power system inertia," in *Proc. 13th Wind Integr. Workshop*, Berlin, Germany, Nov. 2014, pp. 631–638.

[24] M. Dreidy, H. Mokhlis, and S. Mekhilef, "Inertia response and frequency control techniques for renewable energy sources: A review," *Renew. Sustain. Energy Rev.*, vol. 69, pp. 144–155, Mar. 2017.

[25] D. Duckwitz, "Performance of df/dt-based inertia control during emergency islanding," in *Proc. 15th Wind Integr. Workshop*, Vienna, Austria, 2016, pp. 659–663.

[26] D. Duchwitz and B. Fischer, "Modeling and design of *df/dt*-based inertia control for power converters," *IEEE J. Emerg. Sel. Topics Power Electron.*, vol. 5, no. 4, pp. 1553–1564, Dec. 2017.

[27] J. Fang, Y. Tang, H. Li, and X. Li, "A battery/ultracapacitor hybrid energy storage system for implementing the power management of virtual synchronous generators," *IEEE Trans. Power Electron.*, vol. 33, no. 4, pp. 2820−2824, Apr. 2018.

[28] H. Wang and F. Blaabjerg, "Reliability of capacitors for DC-Link applications in power electronic converters−an overview," *IEEE Trans. Ind. Appl.*, vol. 50, no. 5, pp. 3569−3578, Sep./Oct. 2014.

[29] J. Fang, H. Li, Y. Tang, and F. Blaabjerg, "Distributed power system virtual inertia implemented by grid-connected power converters," *IEEE Trans. Power Electron.*, vol. 33, no. 10, pp. 8488−8499, Oct. 2018.

[30] K. Guo, J. Fang, and Y. Tang, "Autonomous DC-link voltage restoration for grid-connected power converters providing virtual inertia," in *Proc. IEEE ECCE*, Portland, Oregon, USA, 23–27 Sep. 2018.

[31] E. Waffenschimidt and R. S. Y. Hui, "Virtual inertia with PV inverters using DC-link capacitors," in *Proc. ECCE Europe*, pp. 1−10, Karlsruhe, Gemany, 5–9 Sep. 2016.

[32] E. Waffenschmidt, "Virtual inertia grid control with LED lamp driver," *Proc. IESC*, pp. 1–6, Cologne, Germany, 30 Jun.–1 Jul. 2016.

[33] S. Yang, J. Fang, Y. Tang, and P. Wang, "Synthetic-inertia-based modular multilevel converter frequency control for improved micro-grid frequency regulation," in *Proc. IEEE ECCE*, Portland, Oregon, USA, 23–27 Sep. 2018.

[34] J. Zhu, C. D. Booth, G. P. Adam, A. J. Roscoe, and C. G. Bright, "Inertia emulation control strategy for VSC-HVDC transmission systems," *IEEE Trans. Power Syst.*, vol. 28, no. 2, pp. 1277-1287, May 2013.

[35] H. Qiu, J. Fang, and Y. Tang, "Explore the capability of power electronic converters in providing power system virtual inertia," in *Proc. IEEE ECCE*, Portland, Oregon, USA, 23–27 Sep. 2018.

[36] M. Liserre, R. Teodorescu, and F. Blaabjerg, "Stability of photovoltaic and wind turbine grid-connected inverters for a large set of grid impedance values," *IEEE Trans. Power Electron.*, vol. 21, no. 1, pp. 263–272, Jan. 2006.

[37] J. L. Agorreta, M. Borrega, J. L´opez, and L. Marroyo, "Modelling and control of N-paralleled grid-connected inverters with LCL filter coupled due to grid impedance in PV plants," *IEEE Trans. Power Electron.*, vol. 26, no. 3, pp. 770–785, Mar. 2011.

[38] B. Wen, D. Boroyevich, R. Burgos, P. Mattavelli, and Z. Shen, "Analysis of D-Q small-signal impedance of grid-tied inverters," *IEEE Trans. Power Electron.*, vol. 31, no. 1, pp. 675–687, Jan. 2016.

[39] J. Fang, X. Li, H. Li, and Y. Tang, "Stability improvement for three-phase grid-connected converters through impedance reshaping in quadrature-axis," *IEEE Trans. Power Electron.*, vol. 33, no. 10, pp. 8365−8375, Oct. 2018.

[40] J. Driesen and K. Visscher, "Virtual synchronous generators," in *Proc. IEEE PESGM*, pp. 1–3, Pittsburgh, USA, 20–24 Jul. 2008.

[41] J. Fang, X. Li, Y. Tang, and H. Li, "Design of virtual synchronous generators with enhanced frequency regulation and reduced voltage distortions", in *Proc. IEEE APEC*, accepted, San Antonio, TEXAS, USA, 4–8 Mar. 2018.

[42] P. F. Frack, P. E. Mercado, M. G. Molina, E. H. Watanabe, R. W. D. Doncker, and H. Stagge, "Control strategy for frequency control in autonomous microgrids," *IEEE J. Emerg. Sel. Topics Power Electron.*, vol. 3, no. 4, pp. 1046–1055, Dec. 2015.

[43] J. Fang, P. Lin, H. Li, Y. Yang, and Y. Tang, "Stability analysis and improvement of three-phase grid-connected power converters with virtual inertia control", in *Proc. IEEE APEC*, Anaheim, CA, USA, 17–21 Mar. 2019.

Jingyang Fang (S'15) received the B.Sc. and M.Sc. degrees in electrical engineering from Xi'an Jiaotong University, Xi'an, China, in 2013 and 2015, respectively, and the Ph.D. degree from the School of Electrical and Electronic Engineering, Nanyang Technological University, Singapore, in 2018.

From May 2018 to August 2018, he was a Visiting Scholar with the Institute of Energy Technology, Aalborg University, Aalborg, Denmark. He is currently a Research Fellow with the School of Electrical and Electronic Engineering, Nanyang Technological University, Singapore. He has published more than 40 papers in the fields of power electronics and its applications, including 16 top-tier journal papers. His research interests include power quality control, stability analysis and improvement,

This article has been accepted for publication in a future issue of this journal, but has not been fully edited. Content may change prior to final publication. Citation information: DOI 10.1109/TPEL.2018.2885513, IEEE Transactions on Power Electronics

renewable energy integration, and digital control in more-electronics power systems.

Dr. Fang was a recipient of the Best Paper Award of Asia Conference on Energy, Power and Transportation Electrification (ACEPT) in 2017 and a recipient of the Best presenter of 2018 IEEE International Power Electronics and Application Conference and Exposition (PEAC) in 2018.

Pengfeng Lin (S'16) received the B.Sc. and M.Sc. degree in electrical engineering from Southwest Jiaotong University, China, in 2013 and 2015 respectively. He is currently working toward Ph.D degree in Interdisciplinary Graduate School, Eri@n, Nanyang Technological University, Singapore.

His research interests include energy storage systems, hybrid AC/DC microgrids and electrical power system stability analyses.

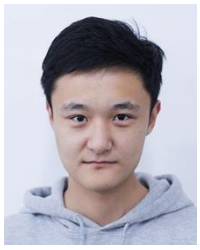

Hongchang Li (S'12−M'16) received the B.Eng. and D.Eng. degrees in electrical engineering from Xi'an Jiaotong University, Xi'an, China, in 2011 and 2016, respectively.

From August 2014 to August 2015, he was a Visiting Scholar with the Molecular Foundry, Lawrence Berkeley National Laboratory, Berkeley, CA, U.S. He is currently a Research Fellow with the Energy Research Institute at Nanyang Technological University, Singapore. His research interests include wireless power transfer, electron tomography and distributed energy storage systems.

Yongheng Yang (S'12-M'15-SM'17) received the B.Eng. degree in electrical engineering and automation from Northwestern Polytechnical University, Shaanxi, China, in 2009 and the Ph.D. degree in electrical engineering from Aalborg University, Aalborg, Denmark, in 2014.

He was a postgraduate student at Southeast University, China, from 2009 to 2011. In 2013, he spent three months as a Visiting Scholar at Texas A&M University, USA. Dr. Yang is currently an Associate Professor with the Department of Energy Technology, Aalborg University. His research focuses on the grid integration of renewable energy, in particular, photovoltaic, power converter design, analysis and control, and reliability in power electronics. He has contributed to two books on the control of power converters and grid-connected photovoltaic systems.

Dr. Yang is an Associate Editor of the IEEE JOURNAL OF EMERGING AND SELECTED TOPICS IN POWER ELECTRONICS (JESTPE), the CPSS Transactions on Power Electronics and Applications, and the Electronics Letters. He was the recipient of the 2018 IET Renewable Power Generation Premium Award.

Yi Tang (S'10−M'14−SM'18) received the B.Eng. degree in electrical engineering from Wuhan University, Wuhan, China, in 2007 and the M.Sc. and Ph.D. degrees from the School of Electrical and Electronic Engineering, Nanyang Technological University, Singapore, in 2008 and 2011, respectively.

From 2011 to 2013, he was a Senior Application Engineer with Infineon Technologies Asia Pacific, Singapore. From 2013 to 2015, he was a Postdoctoral Research Fellow with Aalborg University, Aalborg, Denmark. Since March 2015, he has been with Nanyang Technological University, Singapore as an Assistant Professor. He is the Cluster Director of the Advanced Power Electronics Research Program at the Energy Research Institute, Nanyang Technological University.

Dr. Tang was a recipient of the Infineon Top Inventor Award in 2012, the Early Career Teaching Excellence Award in 2017, and four IEEE Prize Paper Awards. He serves as an Associate Editor for the IEEE Transactions on Power Electronics (TPEL) and the IEEE Journal of Emerging and Selected Topics in Power Electronics (JESTPE).